Peer-reviewed version available at Sensors 2019, 19, 2138; doi:10.3390/s19092138

Fully non-contact hybrid NDT inspection for 3D defect reconstruction using an improved SAFT algorithm

Hossam Selim[1], José Trull[1], Miguel Delgado Prieto[2], Rubén Picó[3], Luis Romeral[2] and Crina Cojocaru[1]

[1] Physics Department, Universitat Politècnica de Catalunya, Rambla Sant Nebridi 22, 08222 Terrassa, Barcelona,Spain;hossam.eldin.mohamed.selim@upc.edu,jose.francisco.trull@upc.edu, crina.maria.cojocaru@upc.edu

[2] Electronic Engineering Department, Universitat Politècnica de Catalunya, Rambla Sant Nebridi 22, 08222 Terrassa, Barcelona, Spain; miguel.delgado@upc.edu , luis.romeral@upc.edu

[3] Instituto de Investigación para la Gestión Integrada de Zonas Costeras,Universitat Politècnica de Valencia, Valencia, Spain, rpico@fis.upv.es

* Correspondence: Rubén Picó[3], rpico@fis.upv.es

Abstract: Non-destructive testing of metallic objects that may contain embedded defects of different sizes is an important application in many industrial branches for quality control. Most of these techniques allow defect detection and its approximate localization, but very few give enough information for its 3D reconstruction. Here we present a hybrid laser – transducer system that combines remote laser-generated ultrasound excitation and non-contact ultrasonic transducer detection. This fully non-contact method gives access to separating scan areas on different object's faces and defect details from different angles/perspectives can be analysed. This hybrid system can analyse the whole object's volume data and allow a 3D reconstruction image of the embedded defects. As a novelty for the signal processing improvement, we use a 2D apodization window filtering technique, applied along with the synthetic aperture focusing algorithm in order to remove the undesired effects of side lobes and wide-angle reflections of propagating ultrasound waves, thus, enhancing the resulting 3D image of the defect. We provide both qualitative and quantitative volumetric results with high accuracy and resolution compared with conventional techniques.

Keywords: laser ultrasonics, non-contact transducers, defects, NDT, SAFT, synthetic aperture, apodization, weighting function, 3D reconstruction

1. Introduction

Non-Destructive Testing (NDT) techniques are widely used for embedded crack detection inside solid materials, with effective results in the quality control and material inspection strategies in modern industry [1]. Ultrasound transducers are considered the most common devices for NDT inspection thanks to their wide frequency band selection, small sizes and ability to work in harsh environments [2,3]. The ultrasound transducers can be used in two major modes of exciter/ receiver operation, namely pulse-echo or pitch-catch modes [4,5]. Depending on the typical application and availability of transducers; either of these two modes is favoured. However, the use of ultrasonic transducers both as exciters as well as receivers of ultrasound has always faced some limitations, including the difficulty to use them in remote applications where it is hard or even impossible to

Peer-reviewed version available at Sensors 2019, 19, 2138; doi:10.3390/s19092138

place the transducer in contact with the object under inspection [6]. The limited resolution and weak generated power of non-contact transducers used as exciters lead to a reduction of the ultrasound waves' penetration depth, limiting their application mostly to the detection of near-surface defects. Non-contact conventional transducers are, however, suitable as receivers. Usual NDT techniques use contact transducers fixed in a single position on the object's surface. Although in contact mode, the received signal has a higher signal to noise ratio (SNR) with higher gain and less attenuation, the contact mode has an important drawback when the same detector has to be used to scan a certain area. When the detector is moved from one point to another, the coupling factor changes, making impossible a quantitative comparison of the two measurements. Moreover, an automatic scanning is not possible to implement with contact sensors. On the contrary, a non-contact transducer can be programmed to automatically scan a larger area, with the drawback of signal attenuation due to the airgap and the weaker sensitivity to detect small variations in the ultrasound signal.

The signal processing usually implemented to contact or non-contact ultrasonic techniques is based on the extraction of the time of flight (TOF) corresponding to the reflected echoes generated by the embedded defects. Several algorithms are proposed in the literature, including the B-scan [7], Fourier transform, short time Fourier transform (STFT) [8], wavelet transform (WT) [9,10], time reversal [11] and synthetic aperture focusing technique (SAFT) algorithms [7,12–15]. Each algorithm has advantages and limitations. For instance, the B-scan algorithm can give time domain and 1D space domain information of the defect by combining multiple A-scan measurements in cascade [13]. The Fourier transform has the ability to detect the frequency response of the detected signal without giving detailed information about the corresponding TOF of a certain frequency component. STFT and WT can detect information about both frequency and TOF with a certain level of uncertainty. However, WT is more flexible and accurate than STFT due to the fact that the window size in the WT changes with frequency and time, whereas the window size, in the case of STFT, is fixed, which limits the resolution of the algorithm [16]. Moreover, time reversal techniques rely on the principle of detecting the ultrasound wave field using a receiver and resending the same wavefield to the source, but reversed in time, producing a convergence of the signal towards the initial source position. If the source of this signal is a defect, then the convergence of the reversed signal will occur at the defect position allowing its visualization. [11]. Finally, the SAFT technique relies on the principle of delay and sum (DAS) that generates a focused image of the defect out of multiple unfocused images. This focused image has a much higher amplitude at the defect position compared with healthy positions inside the object of interest. The SAFT has the advantage of being able to visualize the whole volume providing 2D or 3D information about the object depending on the resolution and the number of scans performed on the object [17]. In the recent literature, the SAFT is used with ultrasonic transducers for generating an image of the embedded defects in the sample under test representing a viable solution for the signal processing [12,14,18].

As an alternative to ultrasonic methods, all-optical systems for ultrasound generation and detection have emerged. Laser generated ultrasound (LGU) technique is used for excitation and optical interferometry setups are used for signal detection. These all-optical methods have a very high resolution and the ability to send and receive signals remotely at a high range of power intensity that is not achievable in the case of conventional transducers [19,20]. This fact implies a higher penetration of the ultrasound to deeper areas inside the object and ability to detect deeper embedded defects. However, the main drawback of the interferometric optical detection, apart from the fact that it is very expensive, is the stability criterion where the system needs to be isolated against surrounding vibrations, making it difficult to apply in practical industrial applications [19]. Due to these drawbacks, all-optical NDT methods are only justified when the defect size is at a micrometre scale.

In this work, we propose a hybrid system which combines laser-induced ultrasound as an exciter and conventional non-contact transducers as a receiver. This method combines the advantages of both technologies to obtain a full contactless 3D reconstruction of a defect with a very good resolution and to improve the feasibility of the system in industrial applications [21]. In the proposed method, both the exciter (the laser spot) and the receiver (only one non-contact transducer) are programmed

Preprints (www.preprints.org) | NOT PEER-REVIEWED | Posted: 16 April 2019 doi:10.20944/preprints201904.0181.v1

Peer-reviewed version available at Sensors 2019, 19, 2138; doi:10.3390/s19092138

to automatically scan 2D surfaces of three different faces of the object under study, which emphasizes the 3D reconstruction of the defect at different perspectives/angles. The recorded ultrasound signals are processed using an improved SAFT algorithm for 3D defect reconstruction. In addition to the SAFT method, an enhanced apodization function is implemented to eliminate the effect of the ultrasound side lobes generated by the exciter as an artifact in the input signal [22]. This technique results in an enhanced quality of the reconstructed image with less redundant or unnecessary shadows. To our knowledge, the apodization function for signal processing using the SAFT algorithm was previously applied to 1D geometries for 2D defect reconstruction. Here, we developed an extended 2D synthetic aperture window apodization function with a volumetric SAFT algorithm as an expansion to the commonly used 1D apodization window in the planar SAFT algorithm [23].

2. Improved SAFT algorithm model

The SAFT algorithm is used in different variations for the signal processing in the NDT technique for the detection of embedded defects. The analysis of the signal can be performed in the time domain or frequency domain. Different setup arrangements have been proposed such as pulse-echo or pitch-catch modes. In the time domain analysis, based on the DAS methodology, the SAFT can provide a focused image of the defect inside the object with a higher SNR than that of other techniques that rely mainly on fewer measurements to detect the presence of a defect. A specific approach has to be considered to create a 3D reconstruction of a volume of interest in order to investigate a particular suspected embedded defect. In this regard, we propose the generation of multiple A-scan measurements at various points with predetermined spacing in both horizontal and vertical directions, creating a 2D scan area. Each of these A-scan signals comprises the superposition of the contribution of individual scatterers inside the active volume of interest. Hence, each time instant at the time scale axis of the A-scan signal is represented by a specific amplitude corresponding to the influence of scatterers that lie inside the active volume at a TOF equivalent to their distance from the exciter-receiver respectively [17]. Figure 1 shows the schematic representation of the 3D object under investigation by an ultrasonic exciter-receiver set in a pitch-catch mode performing the scan on a 2D scan area.

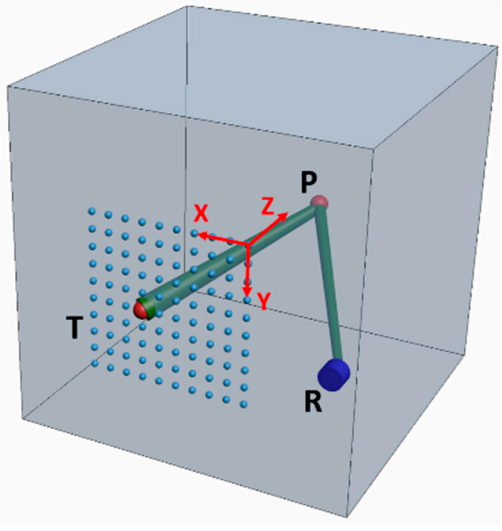

Figure 1: Schematic representation of the 3D object under investigation using the SAFT algorithm.

For an arbitrary excitation point, *T*, that generates an ultrasound wave propagating in the volume and an arbitrary receiver, *R*, which detects the reflected signal by the volume points, one of which is the point of interest, *P*, we can define the TOF of the signal as [12,14,18]:

$$TOF_{(i,j,k)P} = \frac{|\vec{d}_{(i,j,k)P} - \vec{d}_{(i,j,z)T}| + |\vec{d}_{(i,j,k)P} - \vec{d}_{(i,j,z)R}|}{c} \quad (1)$$

Peer-reviewed version available at Sensors 2019, 19, 2138; doi:10.3390/s19092138

where the TOF is the time of flight of the ultrasonic signal generated by the exciter *T*, scattered from the point *P*) and detected by the receiver *R*; $\vec{d}$ is the displacement vector at positions *T*, *R* and *P*, respectively; *i*, *j* and *k* represent the indexes of the volume image points in the *X*, *Y*, *Z* planes respectively; *c* denotes the longitudinal speed of sound in the material of the object.

Shifting the position of the exciter/receiver results in a different TOF for the same particular scatterer in the active volume and a different amplitude at the corresponding time instant at the A-scan signal. The summation of all these amplitudes with respect to their TOFs (Eq.2) will generate a focused image, $y_f(P)$, of that scatter with an overall amplitude corresponding to all scan points in the 2D scan area.

$$y_f(P) = \sum_{j=1}^{N}\sum_{i=1}^{M} y_r(TOF_{(i,j,k)_P}, i, j) \quad (2)$$

where y_r is a preliminary unfocused image of this particular point *P*; y_f is the high-resolution focused image; *M***N* are total scan points in horizontal and vertical directions of the scan area. It must be taken into consideration that Eq.2 does not take into account the effect of the nature of propagating ultrasound in the solid object which mainly contains main lobes and side lobes with different angles and intensities.

In order to reach more accurate results avoiding uncertainties, we propose the use of an apodization function to enhance the resulting image by weighting down the amplitudes that would result from the propagation of side lobes that can produce secondary echoes that influence and distort the main echoes generated by scatterers (Eq.3).

$$y_f(P) = \sum_{j=1}^{N}\sum_{i=1}^{M} a(TOF_{(i,j)_P}, i, j) * y_r(TOF_{(i,j,k)_P}, i, j) \quad (3)$$

where $a(TOF_{(i,j,k)_p}, i, j)$ is the weighting function or apodization function [24]. Eq.3 represents the above idea of DAS where the summation is applied to the delayed versions of the signals at the corresponding scan points. The apodization function is generally chosen to approach zero at the edges of the SA window edges [22].

In the SAFT analysis, if the scan is performed in a line of scan to generate a reconstruction image in a 2D plane, i.e. scan in one line and inspection of the depth of the object in the plane containing that line, we use a 1D apodization window which represents the aperture line at each point of the scatters in the cross-section depth of the object. Extending this to the 3D case, when the SAFT scan is performed in a 2D area to perform a 3D reconstruction image, means that the aperture of the apodization window is also becoming a 2D area. To make it clearer, the dimension of the apodization window is the same as the dimension of the scan line/area as it depends on the position of the scan sensors. A drawback of apodization is the possible change of the main lobe width, which affects the lateral resolution. Hence a good selection of the apodization function and its width helps get the optimum results with a minimum lateral resolution deficiency.

To give a clearer understanding of the apodization function, we will explain this concept shortly in the case of a 1D scan line at X-axis and scatter plane XZ, and later, we will expand the explanation to the general case of 2D scan area and scatterer volume.

For a 1D scan line X-axis and point scatterers in a plane XZ, the width of the apodization function should be proportional to the depth of the scatter point (Figure 2) and it is denoted by Eq.4 below [22]:

$$\Delta X(Z) = 2Z\tan(\Delta\theta_X / 2) \quad (4)$$

where *z* is the depth of the point scatter and $\Delta\theta$ is the angular beam width of the transducer and can be calculated at -6dB based on Eq.5 [25]:

$$\sin(\Delta\theta_X / 2) = 0.514 * \frac{c}{fD} \quad (5)$$

where *f* is the central frequency and *D* is the diameter of the transducer.

The apodization function can be applied to all points falling within a certain normalized X coordinate, $\hat{X}$, and neglecting all other measurements outside this threshold (Eq.6).

$$\hat{X} = \frac{X - X'}{\Delta X(Z)} \tag{6}$$

where X-X′ is the horizontal shift between the position of the scan point and scatterer. The most commonly used types of the apodization function are the rectangular or Hanning function [22]. Eq.7 and Eq.8 represent the rectangular and Hanning windows, respectively, for a 1D scan line on the x-axis [22,23].

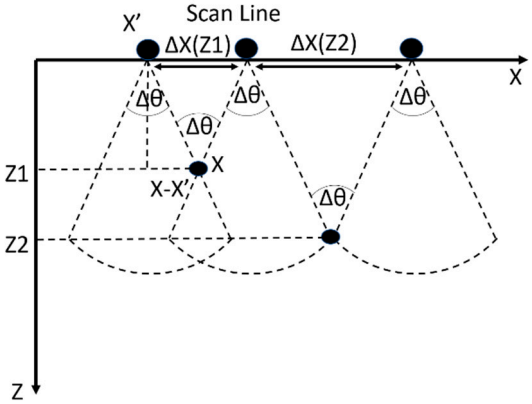

Figure 2: Beamwidth angle $\Delta\theta$ for a point scatterer at depth Z; when the point scatterer is deeper $Z2>Z1$, the synthetic aperture size (ΔX) changes accordingly. The apodization window size should be adapted to the synthetic aperture window size.

$$a(\hat{X})_{rect} = \begin{cases} 1, & |\hat{X}| < \alpha \\ 0, & otherwise \end{cases} \tag{7}$$

$$a(\hat{X})_{Hann} = \begin{cases} 0.5[1 + \cos(\frac{\pi}{\alpha} X)], & |X| < \alpha \\ 0, & otherwise \end{cases} \tag{8}$$

Fine tuning to the threshold criterion value, α, should be applied to obtain the optimum results. In order to apply the same apodization function to the whole volume with a 2D scan area, it is required to put into consideration that the beamwidth angle becomes a solid angle instead of a planar angle. To make it simpler, we will have two angles $\Delta\theta_X, \Delta\theta_Y$ corresponding to the scan area XY instead of the scan line X. In this case, we can deal with the apodization function $a(X,Y)$ as a separable function (i.e. we can calculate the two dimensional function by considering a series of one dimensional functions) [23]. Hence, the one dimensional window functions in Eq.7 and Eq.8 can be transformed into the two dimensional window functions in Eq. 9, Eq.10:

$$a(\hat{r})_{rect} = \begin{cases} 1, & |r| < \alpha \\ 0, & otherwise \end{cases} \tag{9}$$

$$a(\hat{r})_{Hann} = \begin{cases} 0.5[1 + \cos(\frac{\pi}{\alpha} r)], & |r| < \alpha \\ 0, & otherwise \end{cases} \tag{10}$$

where $r = \sqrt{X^2 + Y^2}$ with the introduction of $\hat{Y}$ as the normalized Y coordinate $\hat{Y} = \frac{Y - Y'}{\Delta Y(Z)}$ and $\Delta Y(Z) = 2Z\tan(\Delta\theta_Y / 2)$.

With this generalized case, it is possible to apply the 2D apodization window function to the scan area of interest that would cover the whole volume of interest.

In the derivation of the final image reconstruction using the SAFT technique, it is assumed that the ultrasonic transmitter is small enough to be considered as a point source which is applicable in the case of LGU. Receivers also need to be regarded as a point-like transducer. This means that the smaller the size of the transducer, the less the generated numerical errors in the algorithm.
An important constraint to this algorithm is the limited angle between the transmitter and receiver that typically should not be high to avoid diffraction and side lobe effects (i.e. it should be within the beamwidth of the transducer). Another important constraint is that the dimensions of the object should allow the transmitter scan area and the receiver locations to be far from the object's boundaries to avoid their reflections which result in calculation errors. One other constraint of the SAFT algorithm is that it can work with ultrasonic signals propagating at a single velocity. Thus, the wave dispersion due to working in composite or inhomogeneous materials will result in violating the SAFT algorithm unless the different wave velocities and wave diffractions in different composite structures are taken into consideration.

3. Experimental configuration

The schematic representation of our experimental setup and of the object under study is shown in Figure 3. The experiment was performed on a cubic sample 200 mm^3 made of cast aluminum, with an embedded glass cylinder buried in the cube structure, representing the embedded defect. The cylinder has a 13 mm diameter and a 60 mm height and is positioned vertically inside the cube. The defect was embedded at a depth of 100 mm from the front and side faces (face 1 and 2 in Figure 3b) and 70 mm from the top view of the cube (face 3). It should be noted that due to the fabrication process of the cast aluminum at a high temperature, there is a slight tilting and bending of the glass cylinder. This results in a slight deformation and irregularity of the defect shape and location. Figure 3b also shows the scan areas of 90 x 90 mm^2 at three faces of the cube, with scan points distributed equally in the XY planes of the three faces. Note that, for a simpler signal processing, each face has its own XYZ coordinator system.

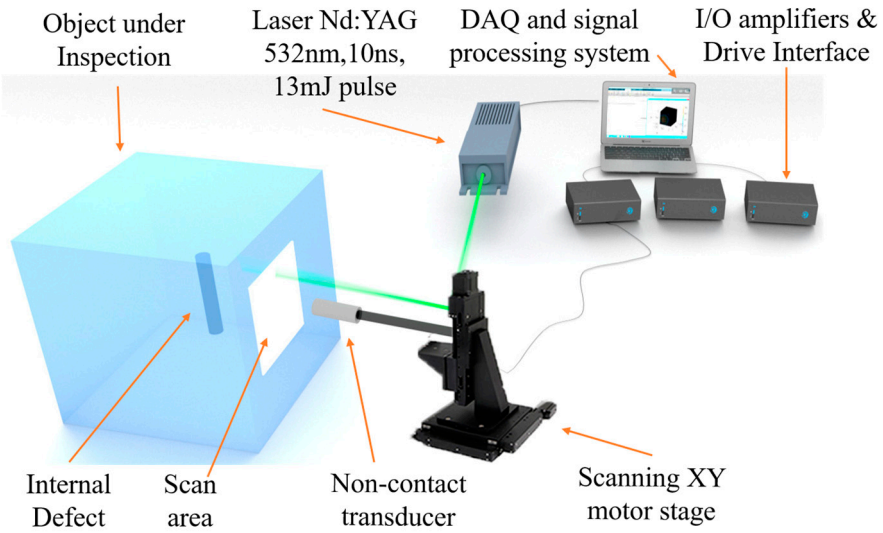

a)

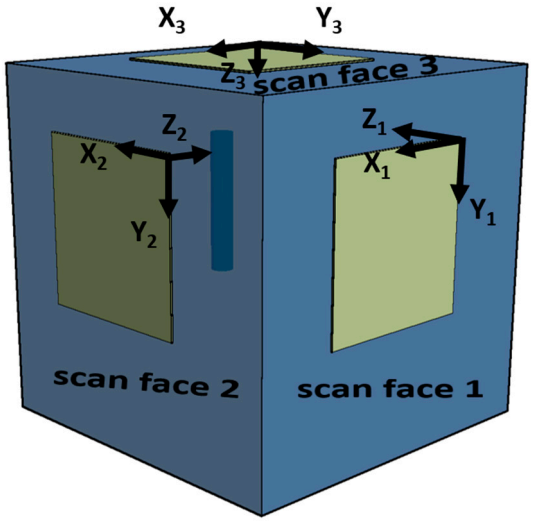

b)

Figure 3: a) Experimental setup used for the excitation and detection of ultrasound waves. b) Schematic representation of the object under study with the three -face scan areas. Different Cartesian axes are represented at each scan face.

For LGU, we used a Nd:YAG laser doubled in frequency, emitting pulses of 8 ns at a wavelength of 532 nm, with an energy per pulse of 10 mJ. The focused laser beam impacts onto the surface of the object under study, where it is rapidly absorbed into a shallow volume of material, creating a localized thermo-elastic expansion. This expansion induces a stress wave generating broadband ultrasound waves that propagate inside the material. The scanning of the laser beam over the selected areas is performed using an XY motorized stage (OSMS CS 26-100X-M6 and OSMS26-100 Z -M6 with controllers HIT_M and HIT-S from manufacturer Optosigma) with a predefined resolution creating a 100x100 scan area points that is equivalent to 90 x 90 mm^2. A software based on Labview and Matlab have been prepared to control the translation stage and to define the scanning areas and number of points. A non-contact transducer (NCT2-D3, Ultran Group) with a nominal frequency of 2 MHz is fixed to the same XY motorized stage that controls the position of the laser beam spot at a fixed vertical spacing of 17 mm from the laser spot. The laser and detector move together in the scanning area. The transducer was placed at a fixed distance of 8.5 mm from the object surface. The signal collected by the sensor is sent to a preamplifier (Olympus 5662), connected to a high-performance Gage A/D card (50 MHz sampling frequency, 16 bit of resolution), linked to a computer for further data processing. For each excitation point, the transducer records a voltage/time (A-scan) data set. We use longitudinal wave detection transducers considering longitudinal ultrasound wave propagation inside the aluminum material at a velocity of 6320 m/s [26,27].

4. Results and discussions

We performed both excitation and detection scan over the three faces of the cube shown in Figure 3b in order to obtain detailed information of the embedded defect at different perspectives/angles, needed for the 3D reconstruction. The captured signals were first subject to the signal conditioning algorithm to obtain a higher quality signal. The algorithm involved filtering and interpolation of the measured signals to remove the noise and low/high frequency components that are of no interest. Additionally, we had a noise signal subtracted from the main signals to remove the background effect. An averaging algorithm was also performed to remove the DC components or offsets in the measured signals. The SAFT algorithm described in section 2 was then applied to all signals coming from the three faces scan areas. It should be noted that a 25 μs time delay, equivalent to the velocity

Preprints (www.preprints.org) | NOT PEER-REVIEWED | Posted: 16 April 2019 doi:10.20944/preprints201904.0181.v1

Peer-reviewed version available at Sensors 2019, 19, 2138; doi:10.3390/s19092138

of ultrasound exiting the object cube at 340 m/s and travelling through the airgap of 8.5 mm towards the transducer, is considered and added to the TOF values extracted from Eq.3. [27]. The Hanning 2D window apodization function was applied to the SAFT algorithm considering the threshold criterion α to be 0.5. A fine-tuning is applied to optimally select the 25 μs time delay and the threshold criterion α in order to get these optimum values that correspond to a sharper image with a high contrast and accuracy.

The results of our full non-contact experiment, for each scan area, are shown in Figure 4. The defect is located and represented for each scan face, at positions corresponding to the higher signal amplitude in the shown figures. The cartesian axes X, Y, Z are chosen for each face to cover only the respective scanned area and have their origin at its top right corner with XY being the scanned area plane and the Z axis is perpendicular to this area. The axes for each face are denoted by X_1, Y_1, Z_1 (face 1), X_2, Y_2, Z_2 (face 2) and X_3, Y_3, Z_3 (face 3), respectively. The results below for the three faces are represented at XY and XZ cross sections respectively. The color map represents the amplitude percentage.

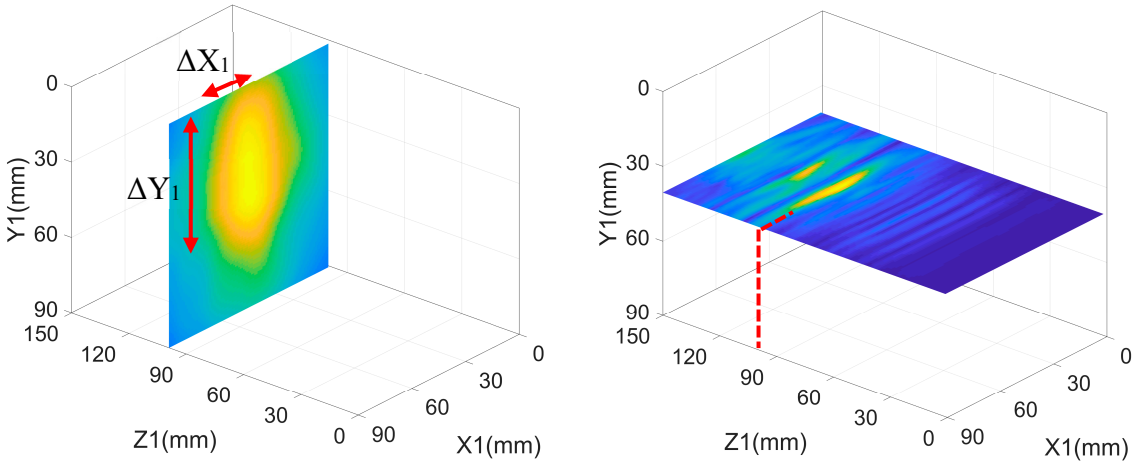

a) b)

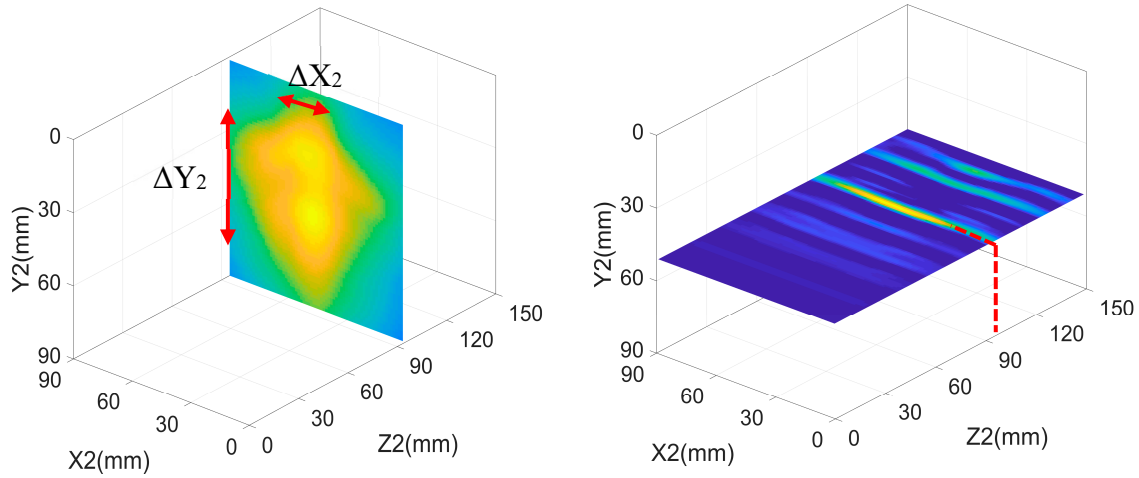

c) d)

Preprints (www.preprints.org) | NOT PEER-REVIEWED | Posted: 16 April 2019 doi:10.20944/preprints201904.0181.v1

Peer-reviewed version available at Sensors 2019, 19, 2138; doi:10.3390/s19092138

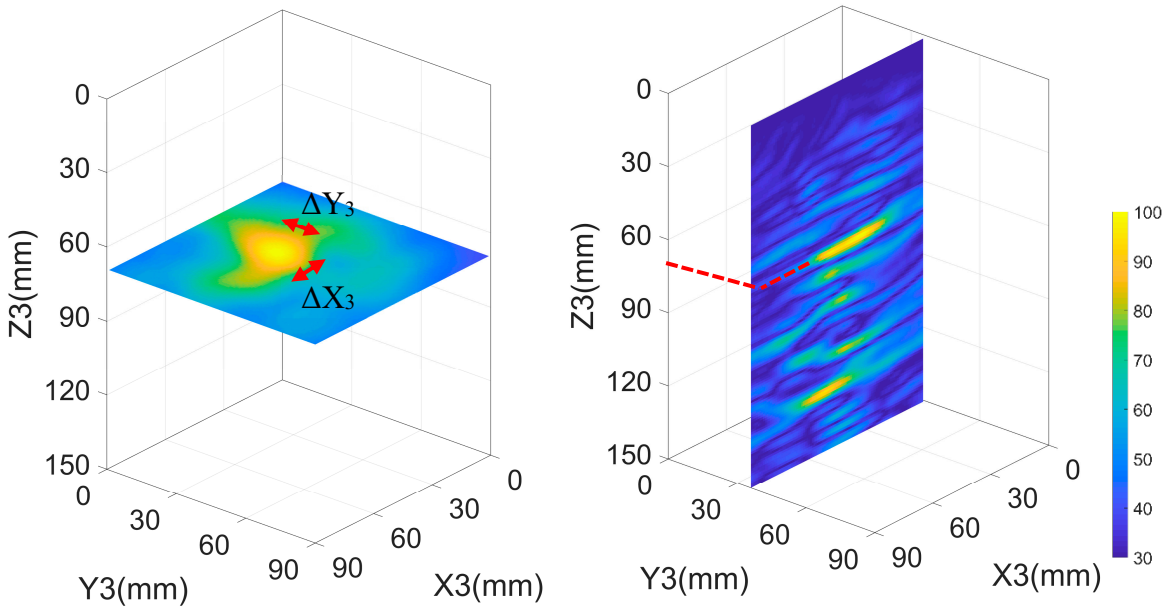

e) f)

Figure 4: The SAFT algorithm results of the three face experiment: a) X_1Y_1 plane slice for face 1 at Z_1 = 99 mm b) X_1Z_1 plane slice for face 1 at Y_1 = 40 mm. c) X_2Y_2 plane slice for face 2 at Z_2 = 95 mm d) X_2Z_2 plane slice for face 2 at Y_2 = 51 mm. e) X_3Y_3 plane slice for face 3 at Z_3 = 70 mm f) X_3Z_3 plane slice for face 3 at Y_3 = 36 mm.

For face 1, we have the front view of the defect in the X_1Y_1 (Figure 4a) and X_1Z_1 (Figure 4b) planes centered at X_1 = 41 mm, Y_1 = 41 mm and at Z_1 = 99 mm. The reconstructed defect dimensions are ΔX_1 = 18 mm, ΔY_1 = 55 mm, which correspond to a size error with respect to the original defect size of $\Delta X_{1,error}$ = 38%, $\Delta Y_{1,error}$ = 8%, and a positioning error of less than 1% in X_1,Y_1 and Z_1 planes where the positioning error refers to the difference between the actual position of the defect's center in X_1,Y_1 and Z_1 planes and the detected ones. With regard to face 2, we see the side view of the defect in the X_2Y_2 and X_2Z_2 planes centered at X_2 = 49 mm, Y_2 = 45 mm and at Z_2 = 95 mm, the detected defect dimensions are ΔX_2 = 19 mm, ΔY_2 = 58 mm. This corresponds to a size error with respect to the original defect size of $\Delta X_{2,error}$ = 46%, $\Delta Y_{2,error}$ = 3% and a positioning error less than 5% in X_2,Y_2 and Z_2 planes. Face3 shows the top view of the defect in the X_3Y_3 and X_3Z_3 planes centered at X_3 = 42 mm, Y_3 = 34 mm and at Z_3 = 70 mm; the detected defect dimensions are ΔX_3 = 16 mm, ΔY_3 = 16 mm, which corresponds to a size error with respect to original defect size of $\Delta X_{3,error}$ = 23%, $\Delta Y_{3,error}$ = 23%, and a positioning error less than 1% in X_3, Y_3 and Z_3 planes. It should be emphasized that the ΔX_{error} magnitude in either face is highly related to the transducer's size, 13 mm in our case. It is not possible for the sensor to accurately measure the size of defects below or equal to the transducer's size. Indeed, the size error ΔY_{error} is small because the defect size in the Y dimension is much higher than the transducer's size. Thus, although the resulting size and positioning estimations obtained from each face show good global performance, the errors can be drastically reduced by using smaller size transducers.

Combining all the three faces views and representing them at the scale of the cube, we may generate the 3D reconstruction of the defect as shown in Figure 5. Here, a unique universal Cartesian axis reference XYZ is used for all the 3 faces with the origin in the corner of the cube object itself. The relative displacement between the scan faces is considered when superimposing the scan faces all together on the 3D reconstruction. We applied a thresholding filter to reject all data below a certain amplitude threshold to keep only the high intensity data to represent the defect position and shape. Applying these reject thresholds with proper fine tuning of the threshold limit also helps reduce the size error since some data with lower intensity is rejected, improving the accuracy of the algorithm. Figure 5a shows the Isometric view resulting from face1 (Front view/X_1Y_1) scan area inspection by

applying a reject threshold for data with an intensity below 65%, while Figure 5b shows the front view resulting from face 1 scan area inspection by applying a reject threshold for data with an intensity below 65%. Figure 5c,d shows the isometric view and side view representations respectively for face 2 with the same threshold condition. Figure 5e,f shows the isometric view and top view representations respectively for face3. Figure 5g shows the isometric view including the intersection between reconstruction results from the three faces with a filtering threshold of intensity reject for values less than 65%. Figure 5h shows the isometric view including the intersection between reconstruction results from the three faces with a more restrictive threshold of intensity to reject data with an intensity below 85%. We superimpose the true cylindrical defect shape on the reconstructed defect images to see how close the detected information is, with respect to true information. It is clear that the detected defect size and position match the true defect size and position. Increasing the number of scanned faces results in a higher resolution reconstruction of the defect from all 360° angles. The reconstructed planes in our case show a high contrast between the points of high intensity (corresponding to the presence of the defect) and the points of low intensity (no defect). The use of the apodization function helped increase this contrast and eliminated the effect of reflections from side lobes or signals at large angles. The size error is enhanced for the case of a threshold of 65% to be less than 10% for the three faces in the horizontal dimension. In the case of 85% threshod , the size error is reduced to be less than 5% in the horizontal dimension. In the vertical dimension, the size error is not affected by a significant change, so it is almost the same error as in the case with no threshold. In our case, the optimum threshold after the fine tuning was 85%, which stronlgy reduced the error in the horizontal dimension.

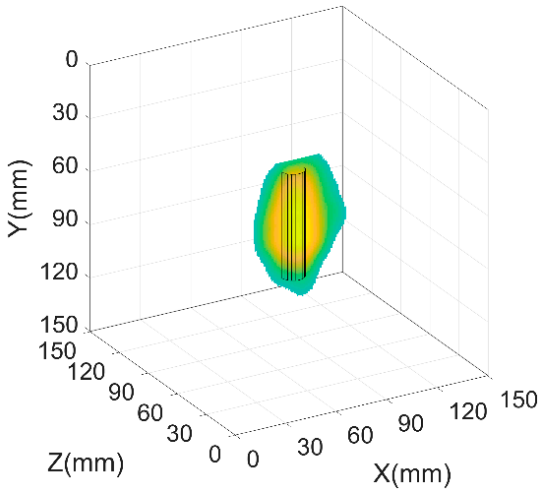

a)

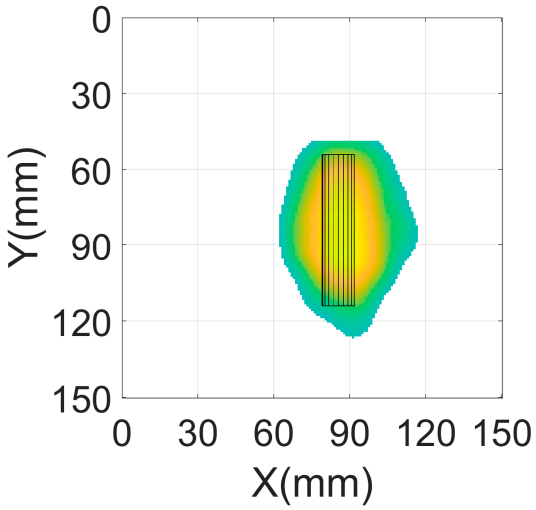

b)

Preprints (www.preprints.org) | NOT PEER-REVIEWED | Posted: 16 April 2019 doi:10.20944/preprints201904.0181.v1

Peer-reviewed version available at Sensors 2019, 19, 2138; doi:10.3390/s19092138

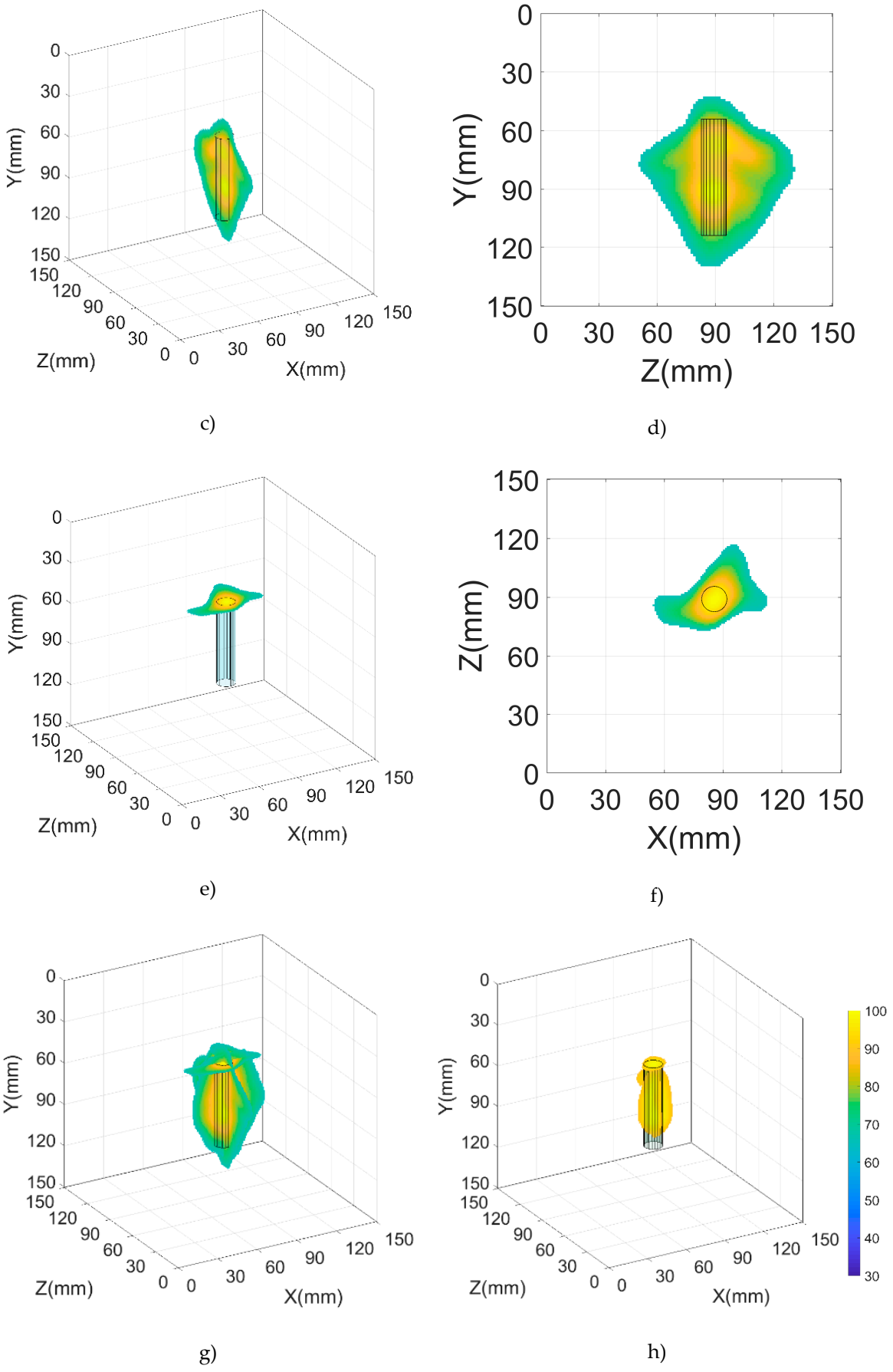

Figure 5: 3D reconstruction of the defect by combining the resulting SAFT images from the three faces and superimposing the actual cylindrical shape of the defect: a) Isometric view resulting from face 1 (front

Peer-reviewed version available at Sensors 2019, 19, 2138; doi:10.3390/s19092138

view/X_1Y_1) scan area inspection by applying a reject threshold for data with an intensity below 65% b) Front view resulting from face 1 scan area inspection by applying a reject threshold for data with intensity below 65% c) Isometric view resulting from face2 (Side view/X_2Y_2) scan area inspection by applying a reject threshold for data with an intensity below 65% d) Side view resulting from face 2 scan area inspection by applying a reject threshold for data with an intensity below 65%e) Isometric view resulting from face3 (Top view/X_3Y_3) scan area inspection by applying a reject threshold for data with an intensity below 65% f) Top view resulting from face 3 scan area inspection by applying a reject threshold for data with an intensity below 65% g) Isometric view resulting from the 3d reconstruction by applying a reject threshold for data with an intensity below 65% h) isometric view by applying a stricter reject threshold for data with an intensity below 85%.

The 3D reconstruction of the defect in Figure 5 clearly shows that the improved SAFT method used in this work has powerful advantages of visualizing the defect in the 3D isometric view. The projections of the SAFT planes make it easier to distinguish the location of the defect in a 3D manner instead of just getting two dimensional results. The SAFT algorithms using a hybrid technique allows scanning over large objects without losing much information. In fact, we get a much better localized quality image of the defect with larger objects compared with smaller ones due to the aforementioned boundary conditions.

The precision of the results obtained here can be further improved using a non-contact transducer with a smaller size, adapted to the horizontal size of the defect. The resolution would be enhanced and calculated accurately with less error. Another significant qualitative enhancement for using the non-contact transducer is the cleaner signal with a higher intensity contrast due to having the receiving transducer closer to the exciter. However; there are also some drawbacks for using the non-contact transducer. For example, positioning the non-contact transducer close to the exciter is obligatory, otherwise, there would be much attenuation in the received signal and it will be very difficult to detect the presence of embedded defects. Also, the airgap affects the quality of the signal, but this is rectified in our experiment by using a high-power pulsed laser exciter and high-gain preamplifier.

An important advantage of the proposed method is that there is no need to use a healthy reference sample for comparison with the resulting reconstruction image of the unhealthy sample to detect the presence of the defects. However, in the case of an object that has no symmetrical dimensions or has a composite structure of different materials, it would be better to use the healthy reference sample. This is because the internal reflections of the internal boundaries inside the object can be misinterpreted as a defect while they, in fact, represent the object structure.

5. Conclusion

We have proved that using a hybrid method composed by LGU, as an exciter, and non-contact transducer, as a detector, we can design a fully non-contact configuration for the NDT inspection and 3D reconstruction of a defect embedded in a metallic object. The use of LGU allows the remote excitation of large scan areas with a higher level of power that is not achievable with conventional transducers and this helps penetrate the ultrasound signal to detect embedded defects more efficiently. On the other hand, non-contact transducers have the advantage of having a large number of points scan and proximity to the exciter, which allows the detection of more details of the reflected ultrasound waves. The combination of signals coming from three orthogonal scanning areas of the object detect the defect's presence from all perspectives/angles. An improved SAFT algorithm is implemented to localize the defect position with a signal to noise ratio, taking into consideration the limitations of structural dimensions. The SAFT algorithm provides more information about the exact location of the defect using 3D reconstruction imaging. The use of the 2D apodization technique helped enhance the SNR ratio and reject the effect of side lobes excited along with the main ultrasound lobes as well as the effect of wide angle reflections. The hybrid fully non-contact

techniques presented here provide a strong alternative to conventional NDT techniques with higher flexibility, higher resolution and powerful detection of embedded defects.

Author Contributions:

Conceptualization, Hossam Selim , Miguel Delgado Prieto, Luis Romeral and Crina Cojocaru ; Data curation, Hossam Selim ; Formal analysis, Hossam Selim; Funding acquisition, Luis Romeral and Crina Cojocaru ; Investigation, Hossam Selim ; Methodology, Hossam Selim, Miguel Delgado-Prieto and Crina Cojocaru; Project administration, Luis Romeral and Crina Cojocaru ; Resources, José Trull and Rubén Picó Vila; Software, Hossam Selim and Miguel Delgado-Prieto; Supervision, Miguel Delgado-Prieto, José Trull, Rubén Picó Vila, Luis Romeral and Crina Cojocaru; Validation, Hossam Selim, Miguel Delgado-Prieto, José Trull Rubén Picó Vila and Crina Cojocaru; Visualization, Hossam Selim ; Writing – original draft, Hossam Selim and Crina Cojocaru; Writing – review & editing, Miguel Delgado, Rubén Picó Vila, Luis Romeral, José Trull and Crina Cojocaru.

Conflicts of Interest: The authors declare no conflict of interest. The funders had no role in the design of the study; the collection, analyses, or interpretation of data; the writing of the manuscript, or the decision to publish the results.

Acknowledgement: The work was supported by Spanish Ministry of Economy and Innovation (MINECO) and European Union FEDER through project FIS2015-65998-C2-1 and FIS2015-65998-C2- 2 and by project AICO/2016/060 by Consellería de Educación, Investigación, Cultura y Deporte de la Generalitat Valenciana.

H. Selim, J. Trull and C. Cojocaru acknowledge partial support from US Army Research, Development and Engineering Command (RDECOM) through project W911NF-16-1-0563.

References

1. Her, S.-C.; Lin, S.-T. Non-Destructive Evaluation of Depth of Surface Cracks Using Ultrasonic Frequency Analysis. *Sensors* **2014**, *14*, 17146-17158.
2. Mi, B.; Michaels, J.E.; Michaels, T.E. An ultrasonic method for dynamic monitoring of fatigue crack initiation and growth. *J. Acoust. Soc. Am.* **2006,** 119(1):74-85.
3. Cheng, Y.; Deng, Y.; Cao, J.; Xiong, X.; Bai, L.; Li, Z. Multi-wave and hybrid imaging techniques: A new direction for nondestructive testing and structural health monitoring. *Sensors* **2013**; *13*, 16146-16190.
4. Delrue, S.; Van Den Abeele, K.; Blomme, E.; Deveugele, J.; Lust, P.; Matar, O.B. Two-dimensional simulation of the single-sided air-coupled ultrasonic pitch-catch technique for non-destructive testing. *Ultrasonics* **2010,** *50*, 188–196.
5. Delrue, S.; Tabatabaeipour, M.; Hettler, J.; Van Den Abeele, K. Applying a nonlinear, pitch-catch, ultrasonic technique for the detection of kissing bonds in friction stir welds. *Ultrasonics* **2016**, *68*, 71–79.
6. Bai, Z.; Chen, S.; Xiao, Q.; Jia, L.; Zhao, Y.; Zeng, Z. Compressive sensing of phased array ultrasonic signal in defect detection: Simulation study and experimental verification. *Struct. Heal. Monit.* **2017,** 17(2):147592171770146.
7. Tiwari, K.A.; Raisutis, R.; Tumsys, O.; Ostreika, A. Defect Estimation in Non-Destructive Testing of Composites by Ultrasonic Guided Waves and Image Processing. *electronics* **2019**, *8*, 315.
8. Le, M.; Kim, J.; Kim, S.; Lee, J. Nondestructive testing of pitting corrosion cracks in rivet of multilayer structures. *Int. J. Precis. Eng. Manuf.* **2016**, *17*, 1433–1442.
9. Praveen, A.; Nikhilesh; Vijayarekha, K.; Manjula, K.; Venkatraman, B. Wavelet analysis and de-noising of signal. *Res. J. Appl. Sci. Eng. Technol.* **2012**, *4*, 5534–5538.
10. Selim, H.; Delgado Prieto, M.; Trull, J.; Romeral, L.; Cojocaru, C. Laser Ultrasound Inspection Based

on Wavelet Transform and Data Clustering for Defect Estimation in Metallic Samples. *Sensors (Basel).* **2019**, *19,* 573.

11. Prada, C.; Kerbrat, E.; Cassereau, D.; Fink, M. Time reversal techniques in ultrasonic nondestructive testing of scattering media. *Inverse Probl.* **2002**, *18*, 1761–1773.
12. Spies, M.; Rieder, H.; Dillhöfer, A.; Schmitz, V.; Müller, W. Synthetic Aperture Focusing and Time-of-Flight Diffraction Ultrasonic Imaging — Past and Present. **2012**, 310–323.
13. Tiwari, K.A. Hybrid Signal Processing Technique to Improve the Defect Estimation in Ultrasonic Non-Destructive Testing of Composite Structures. *Sensors* **2017,** *17*(12), 2858.
14. Boonsang, S.; Zainal, J.; Dewhurst, R.J. Synthetic aperture focusing techniques in time and frequency domains for photoacoustic imaging. *Insight Non-Destructive Test. Cond. Monit.* **2004**, *46*, 196–199.
15. Guarneri, G.A.; Pipa, D.R.; Neves, F.J.; de Arruda, L.V.R.; Zibetti, M.V.W. A sparse reconstruction algorithm for ultrasonic images in nondestructive testing. *Sensors (Switzerland)* **2015**, *15*, 9324–9343.
16. Gómez, M.; Castejón, C.; García-Prada, J. Review of Recent Advances in the Application of the Wavelet Transform to Diagnose Cracked Rotors. *Algorithms* **2016**, *9*, 19.
17. Selim, H.; Delgado, M.; Trull, J.; Picó, R.; Cojocaru, C. Material Defect Reconstruction by Non-Destructive Testing with Laser Induced Ultrasonics. *J. Phys. Conf. Ser.* **2018**, *1149*.
18. Stepinski, T. Synthetic aperture focusing techniques for ultrasonic imaging of solid objects. *Synth. Aperture Radar* **2010**, 438–441.
19. Kreis, T. Application of Digital Holography for Nondestructive Testing and Metrology: A Review. *IEEE Trans. Ind. Informatics* **2016**, *12*, 240–247.
20. Zhang, K.; Zhou, Z.; Zhou, J. Application of laser ultrasonic method for on-line monitoring of friction stir spot welding process. *Appl. Opt.* **2015**, *54*, 7483–7489.
21. Jen, C.; Wu, K. NDE using laser generated ultrasound and integrated ultrasonic transducer receivers. *Ultrason. Symp.* **2008**, 1516–1519.
22. Martin, H.S. Synthetic aperture ultrasound imaging with application to interior pipe inspection. *Univ. Tromsø* **2012**, 1–135.
23. Widada, W. Two Dimensional Window Functions, Naval Postgraduate School, 1979.
24. Jensen, J.A.; Nikolov, S.I.; Gammelmark, K.L.; Pedersen, M.H. Synthetic aperture ultrasound imaging. *Ultrasonics* **2006**, *44*.
25. *Ultrasonic Transducers*; Vol. Pana_UT_EN; Olympus Corporation, URL: http://www.epsilon-ndt.com/upload/file/problar-ve-aksesuarlar-.pdf
26. Cong, S.; Zhang, W.W.; Zhang, J.Y.; Gang, T. Analysis on Ultrasonic TOFD Imaging Testing for Ultra-thick-walled EBW Joint of Aluminum Alloy. In Proceedings of the Procedia Engineering; 2017; Vol. 207, pp. 1910–1915.
27. Wang, X.G.; Wu, W.L.; Huang, Z.C.; Chang, J.J.; Wu, N.X. Research on the transmission characteristics of air-coupled ultrasound in double-layered bonded structures. *Materials (Basel).* **2018**, *11*(2): 310.